Characterization of the three-dimensional synaptic and mitochondrial nanoarchitecture within glutamatergic synaptic complexes in postmortem human brain via focused ion beam-scanning electron microscopy

Jill R. Glausier[1]^, Cedric Bouchet-Marquis[2], Matthew Maier[1], Tabitha Banks-Tibbs[1,3,4], Ken Wu[2], Jiying Ning[1], Darlene Melchitzky[1], David A. Lewis[1], and Zachary Freyberg[1,5]

[1]Department of Psychiatry, University of Pittsburgh; [2]Materials and Structural Analysis, Thermo Fisher Scientific; [3]Department of Human Genetics, University of Pittsburgh; [4]College of Medicine, The Ohio State University; [5]Department of Cell Biology, University of Pittsburgh

^Corresponding Author

Contact E-mail: Glausierjr@upmc.edu

Current address: University of Pittsburgh, Department of Psychiatry, Pittsburgh, PA 15213

ABSTRACT

Glutamatergic synapses are the primary site of excitatory synaptic signaling and neural communication in the cerebral cortex. Electron microscopy (EM) studies in non-human model organisms have demonstrated that glutamate synaptic activity and functioning are directly reflected in quantifiable ultrastructural features. Thus, quantitative EM analysis of glutamate synapses in *ex vivo* preserved human brain tissue has the potential to provide novel insight into *in vivo* synaptic functioning. However, factors associated with the acquisition and preservation of human brain tissue have resulted in persistent concerns regarding the potential confounding effects of antemortem and postmortem biological processes on synaptic and sub-synaptic ultrastructural features. Thus, we sought to determine how well glutamate synaptic relationships and nanoarchitecture are preserved in postmortem human dorsolateral prefrontal cortex (DLPFC), a region that substantially differs in size and architecture from model systems. Focused ion beam-scanning electron microscopy (FIB-SEM), a powerful volume EM (VEM) approach, was employed to generate high-fidelity, fine-resolution, three-dimensional (3D) micrographic datasets appropriate for quantitative analyses. Using postmortem human DLPFC with a 6-hour postmortem interval, we optimized a tissue preservation and staining workflow that generated samples of excellent ultrastructural preservation and the high-contrast staining intensity required for FIB-SEM imaging. Quantitative analysis of sub-cellular, sub-synaptic and organelle components within glutamate axo-spinous synapses revealed that ultrastructural features of synaptic function and activity were well-preserved within and across individual synapses in postmortem human brain tissue. The synaptic, sub-synaptic and organelle measures were highly consistent with findings from experimental models that are free from antemortem or postmortem effects. Further, dense reconstruction of neuropil revealed a unique, ultrastructurally-complex, spiny dendritic shaft that exhibited features characteristic of neuronal processes with heightened synaptic communication, integration and plasticity. Altogether, our findings provide a critical proof-of-concept that *ex vivo* VEM analysis provides a valuable and informative means to infer *in vivo* functioning of human brain.

INTRODUCTION

Coordinated, adaptable synaptic signaling underlies core brain processes, such as thought, emotion, learning and memory[1]. Loss or dysfunction of synaptic signaling is thought to be the pathophysiological substrate for severe brain disorders such as schizophrenia[2,3] and autism spectrum disorder[4], which are characterized by impairments to these core brain processes. Thus, investigating synaptic signaling in the human brain is critical to advance the understanding of both normal synaptic function and the nature of synaptic dysfunction in disease.

The morphological substrate of synaptic communication is the synaptic complex[5,6], comprised in its most elemental form by a presynaptic axonal bouton and a postsynaptic element such as a dendritic spine. The synaptic complex and its constituent components can be directly visualized in human brain tissue with electron microscopy (EM) approaches. A substantial literature in experimental, non-human model organisms demonstrates that *in vivo* synaptic function, particularly in the glutamate system, is directly reflected in ultrastructural measures obtained *ex vivo* via EM. For example, presynaptic active zone size reflects the relative level of axonal bouton activation and glutamate release probability[7-11]. The postsynaptic density (PSD) size is strongly correlated with excitatory postsynaptic potential amplitude[7] and abundance of AMPA receptors[12-16]. Because synaptic communication represents the largest energy-demanding process in the brain[17-26], relative ATP demand is reflected by the abundance[25,27,28], size[27,29] and morphology[30-33] of mitochondria within synaptic complexes. Moreover, a fundamental feature of synaptic communication is that pre- and postsynaptic elements act together as a functional unit[34,35], and EM ultrastructural measures also capture this core aspect of synaptic functioning[36]. For example, presynaptic glutamate release probability and presynaptic active zone size correlate with PSD size[7,8]. Likewise, presynaptic mitochondrial abundance is related to PSD size[33,37]. Thus, the intrinsic coupling of synaptic function and ultrastructure demonstrates that valuable insights into *in vivo* synaptic function could be derived from quantitative EM analysis of *ex vivo* preserved human brain tissue. However, whether these synaptic function-ultrastructure relationships are present in human brain is unclear.

Human brain tissue is sourced either from biopsies obtained during neurosurgical interventions or from donations obtained postmortem. However, postmortem donations are the exclusive source for brain tissue from individuals unaffected by brain disorders during life and for individuals with disorders like schizophrenia and autism spectrum disorder, which are currently not diagnosed or treated via neurosurgery. Because whole, intact brains are typically obtained, postmortem sources also permit analysis of multiple brain regions from a single subject, as well as analysis of regions not typically obtained during neurosurgery. For example, the dorsolateral prefrontal cortex (DLPFC) is a higher-order, multi-modal association area[38,39] that is uniquely expanded in humans[40,41], and is considered a key site of synaptic dysfunction in human-specific psychiatric disorders[42-45]. EM analysis of DLPFC obtained postmortem presents a unique opportunity to investigate synaptic and sub-synaptic impairments present in individuals with psychiatric disorders relative to individuals unaffected by brain disorders. Although EM studies of postmortem human DLPFC have been published (for examples see[46-49]), these utilized a conventional two-dimensional (2D) approach to study single ultrathin (~60nm) sections in order to generate estimates of three-dimensional (3D) features. Furthermore, a Z resolution of ~60nm may obscure some ultra- and nanostructures, even when ultrathin sections are studied in series. Finally, serious concerns persist

regarding potential confounding effects of postmortem biological processes on synaptic and sub-synaptic ultrastructural features.

The primary goal of this study was to employ a new strategy to determine how well synaptic nanoarchitecture and relationships are preserved in postmortem human brain, within the context of the surrounding neuropil[50]. We performed a quantitative, 3D ultrastructural analysis of glutamate synaptic complexes in postmortem human DLPFC using focused ion beam-scanning electron microscopy (FIB-SEM). This volume electron microscopy (VEM) approach works by using a focused ion beam to remove a sub-10 nm slice of the tissue, then captures images of the newly-exposed cross-section face via SEM[51]. By iterating through these steps, a 3D volume of brain tissue is acquired with fine Z resolution. Using this innovative technology, we imaged and densely-reconstructed a volume of DLPFC with essentially no loss of information at a 5nm milling step-size from an individual with no brain disorders present during life. We also completed targeted, 3D reconstructions and volumetric analyses of 50 Type 1 axo-spinous glutamatergic synapses. Quantitative analyses revealed that the fundamental relationships between pre- and postsynaptic components identified in non-human experimental systems is clearly evident in postmortem human brain tissue. Furthermore, dense reconstruction of DLPFC neuropil revealed novel structural organization within the human DLPFC, including a spiny dendritic segment that exhibited unique and complex ultrastructural features indicative of heightened synaptic communication. Overall, our findings provide a critical proof-of-concept that *ex vivo* VEM analysis offers a valuable and informative means to infer *in vivo* functioning of individual synaptic complexes in human brain.

METHODS

Human Subject.

The brain specimen was obtained during a routine autopsy conducted at the Allegheny County Office of the Medical Examiner (Pittsburgh, PA) after consent for donation was obtained from the next-of-kin. An independent committee of experienced research clinicians confirmed the absence of any lifetime psychiatric or neurologic diagnoses for the decedent based on medical records, neuropathology examinations, toxicology reports, and structured diagnostic interviews conducted with family members of the decedent[52,53]. This subject was a 62-year-old male who died suddenly and out-of-hospital with an accidental manner of death. The postmortem interval (PMI, defined as the time elapsed between death and brain tissue preservation) was 6.0 hours. PFC pH was measured as 7.0, and RNA Integrity Number measured as 8.7. These demographic and tissue features are within the range of our previously published light and electron microscopic studies of postmortem human brain tissue[46,48,49,54]. All procedures were approved by the University of Pittsburgh's Committee for the Oversight of Research and Clinical Training Involving Decedents and the Institutional Review Board for Biomedical Research.

Tissue Preparation.

A tissue block approximately 1 cm^3, containing cortical layers 1-6 and the underlying white matter, was dissected from the fresh middle frontal gyrus, Brodmann Area 46 (**Figure 1A-B**). The tissue block was immersed in a solution of 4% paraformaldehyde and 0.2% glutaraldehyde in PBS for 24 hours at room temperature,

followed by 24 hours at 4^0C in fresh fixative. The fixed tissue block was sectioned with a 50 μm step-size on a vibratome (VT 1000P, Leica, Wetzlar, Germany), and sections were stored in a cryoprotectant solution (30% ethylene glycol and 30% glycerol) at -30^0C until time for histological processing. Images and data presented in the current manuscript were obtained from a tissue slice that was stored in these conditions for 8.15 years.

Tissue sections were processed using an approach modified from Hua et al[55]. As described above, our approach for tissue extraction, fixation, sectioning and preservation substantially differed from the original protocol. We also introduced modifications to the dehydration and embedding steps, including dehydration at room temperature, use of propylene oxide as the final dehydrant, and employing a different resin mixture (Electron Microscopy Sciences [EMS], Hatfield, PA, USA) containing EMbed 812, Araldite GY 502, DDSA (Dodecenyl Succinic Anhydride) and BMDA (N-Benzyl-N, N-Dimethylamine). After infiltration with 100% resin, tissue sections were mounted onto glass slides coated with liquid release agent (EMS), and set at 60^0C for 48 hours to allow resin polymerization. These modifications preserved the benefits of the Hua et al[55] approach, including a staining intensity of sufficiently high contrast to visualize neuropil components via FIB-SEM and maintenance of staining intensity throughout the depth of the tissue section, while demonstrating that modifications to sample preparation and embedding are compatible with the original protocol.

Sample Preparation and Screening.

Tissue sections were visualized using a dissecting microscope. A ~2mm x 2mm sample of cortical layer 3 (**Figure 1C**) was dissected and adhered to a resin capsule. Using a Leica Ultracut UCT ultramicrotome, excess resin was trimmed with a diamond knife (Histo Diamond Knife, Diatome, Switzerland) until the face of the tissue was visible. Using a standard trapezoid approach and an Ultra 45° diamond knife (Diatome), silver sections were collected onto Formvar-coated copper slot grids (EMS) and examined on a JEOL JEM 1011 transmission electron microscope (JEOL Ltd., Tokyo, Japan) to confirm tissue was present.

FIB-SEM Imaging.

The tissue sample was milled and imaged using a Helios 5 CX FIB-SEM (Thermo Fisher Scientific). After mounting onto the SEM stub using silver paste, the sample was coated with 5nm Ir for enhanced conductivity. Front and side trenches were milled for cross section imaging, and electron beam and ion beam fiducial markers were prepared for milling and imaging alignment. Milling and imaging were carried out at a 52° stage tilt in an automated manner using the Thermo Scientific Auto Slice and View 4.2 Software package. Milling conditions were 30kV, 0.43 nA for a 5 nm slice thickness. The final high-resolution imaging was performed at 2 kV, 0.4 nA with 4 μs dwell time at a 4055 x 3278 image dimension. A total number of 1,580 slices were acquired at 5 nm isotropic voxels to generate a complete volume of 2,630 μm^3 with dimensions 20.3 x 16.4 x 7.9 μm. Acquired image stacks were aligned and segmented using Thermo Scientific Amira Software.

Ultrastructural Analysis.

A sub-volume of neuropil (64.2 μm^3 with dimensions 6275 x 4095 x 2500 nm) that excluded cell bodies and vascular structures was extracted from the master volume and underwent dense reconstruction of neuronal

and astrocyte processes (**Figure 1D-E**) using a semi-automated approach with Amira software. In brief, the plasma membrane of each structure was manually segmented in the first, middle and last ortho-slices. The Interpolation deep-learning module was then applied to segment the remaining plasma membrane of the structure. The operator evaluated, and corrected where needed, the semi-automated segmentation. This approach generated a 3D reconstruction of each structure within the sub-volume. Structures were annotated as a neuronal dendritic shafts, dendritic spines, axonal boutons, unmyelinated axons, myelinated axons, or astrocyte processes using well-established ultrastructural criteria[56-60].

Type 1 glutamatergic synapses (**Figure 2**) were defined by a presynaptic axonal bouton directly apposed to a postsynaptic element. The postsynaptic element possessed a PSD, the electron-dense region characteristic of glutamate synapses that contains the postsynaptic proteins required for glutamatergic synaptic signaling[61]. The presynaptic bouton possessed a presynaptic active zone, defined as the electron-dense and synaptically-engaged region of the axonal bouton[62]. The pre- and postsynaptic compartments were separated by a distinct synaptic cleft[56]. Type 2, non-glutamatergic synapses were identified as described above, except the postsynaptic element did not contain a PSD, but instead exhibited greater plasma membrane electron density in the area apposed to the bouton relative to surrounding membrane. Type 1 and Type 2 synaptic densities were calculated in the densely-reconstructed sub-volume (64.2 μm^3).

A targeted analysis of 50 Type 1 axo-spinous synapses was separately completed to obtain detailed volumetric measurements of synaptic and sub-synaptic components. Because the entirety of the synapse was required to be present in X, Y and Z dimensions for this analysis, the master volume was evaluated for Type 1 synapses. Using a random Z-plane start, 50 Type 1 axo-spinous synapses were identified in the X dimension using the above criteria. The axonal bouton, spine head, presynaptic active zone and PSD were fully reconstructed in 3D to obtain individual ultrastructural volumes.

Each Type 1 axo-spinous synapse was also evaluated for the presence of presynaptic mitochondria in boutons and a postsynaptic spine apparatus in spines. Mitochondria are discrete organelles identified by well-established ultrastructural criteria[57,63], including the presence of a double membrane, internal cristae and matrix. Mitochondrial abundance[25,27,28], size[27,29] and morphology[30-33] inform the relative level of activity at individual synapses[64,65]. The number of presynaptic mitochondria was tallied, and the volume of each was obtained via 3D reconstruction. All mitochondria were classified as exhibiting globular, elongated, toroid (*i.e.*, doughnut-shaped) or damaged morphology[30,48,66]. Globular and elongated morphologies are characteristic of intact and functional mitochondria in high and low energy states, respectively. Toroid and damaged morphologies are associated with mitochondrial dysfunction *per se*[67,68]. Finally, each dendritic spine was evaluated for the presence of a spine apparatus. Spine apparatuses represent an extension of smooth endoplasmic reticulum (SER) into the spine head, and are present in dendritic spines that are more synaptically active[69,70]. A spine apparatus appears as discrete tubular or vesicular structures within the spine head[71,72].

Statistics.

All statistical analyses were completed using SPSS software (version 27, IBM, Armonk, NY). Pearson correlation coefficient analyses were used to assess linear relationships between structure volumes. Fishers

exact test was used to test whether the presence of mitochondria or a spine apparatus differed across synaptic populations. One-way ANOVA was used to test differences in synaptic compartment and organelle volumes between synaptic populations.

RESULTS

Qualitative Assessment of VEM-Imaged DLPFC Layer 3 Neuropil Volume.

The 3D VEM dataset of postmortem human DLPFC layer 3 exhibited excellent ultrastructural preservation[48] (**Figure 3**; Supplemental Videos 1-2). Cellular and organelle plasma membranes were intact, and these structures had a paucity of swelling, deformation or other signs of autolysis. Neuronal compartments such as axonal boutons, dendritic shafts and spines, and axons were clearly identifiable. Consistent with the cytoarchitectonic characteristics of DLPFC layer 3, axonal processes were almost exclusively unmyelinated, likely reflecting glutamatergic pyramidal neuron intrinsic or associational collaterals[73-75]. Mitochondria exhibited ultrastructural features characteristic of preserved integrity, including organized cristae, homogenous matrix, and globular or elongated morphology[30,48,66] (**Figure 4**). Consistent with the association of distinct mitochondrial morphologies with high or low energy states, the globular mitochondrion is present in an axon terminal forming a synapse (**Figure 4A**), whereas the elongated mitochondrion is present in an axon terminal lacking a synapse (**Figure 4C**). Additionally, reconstructed cristae in the globular mitochondrion are large, spanning much of the mitochondrial volume, whereas the cristae in the elongated mitochondrion are truncated. Indeed, the calculated cristae:matrix volume ratio is 0.7 for the globular mitochondrion and 0.4 for the elongated.

Synaptic complexes were readily detected in the 3D neuropil volume. Sub-synaptic structures in Type 1 synapses, such as active zones, synaptic vesicles and PSDs, were clearly identifiable (**Figures 5-6**). Dendritic spines were typically the recipient of Type 1 synapses, and these spines often contained a spine apparatus (**Figure 7A-B**). As expected, mitochondria were not observed in synaptic spine heads, but were present in the dendritic shaft near the base of the spine neck (**Figure 7B**). In addition to spines, Type 1 synapses were also formed on dendritic shafts (**Figure 7C**). Type 2 synapses, presumably GABAergic, were identified on neuronal somata (**Figure 7D**). We also observed dually-innervated spines receiving a Type 1 and a Type 2 synapse (**Figure 7E-F**). Finally, vesicular structures tethered to the outer membrane of presynaptic mitochondria were occasionally observed (**Figure 7E-F**).

Distinct sub-cellular structures situated within the cytoplasm of dendritic shafts, as if piercing through the dendrite, were also observed. To further investigate these invaginating structures, a pyramidal neuron dendritic shaft, all spines emerging from the shaft, and the sub-cellular structures coursing through the shaft cytoplasm were reconstructed (**Figures 8-9**). The parent dendritic shaft segment spanned all 1,580 ortho-slices (7.9 μm) in the Z dimension, had a mean spine occurrence of 0.5/μm, and a total volume of 2.0 μm^3 (**Figure 8A**). Four distinct, cylindrical structures were completely engulfed by the dendrite, and unexpectedly, did not connect to any parent structure (**Figure 8B**). On average, these structures spanned 1.7 ± 0.55 μm in the Z direction, had a diameter of 295.4 ± 77.0 nm and volume of 0.12 ± 0.68 μm^3. The plasma membranes of these invaginating structures were clearly differentiated from the plasma membrane surrounding the dendritic cytoplasm, and the two membranes exhibited multiple areas which resembled non-synaptic puncta adhaerens[57] (**Figure 9**). The size

and ultrastructural appearance of these structures resemble those of dendritic and axonal filopodia[76,77]. Notably, the presence of invaginated structures within dendritic shafts is consistent with recent reports using human PFC[78] or temporal lobe[79] biopsy samples for VEM.

This complex parent dendrite exhibited other distinctive ultrastructural features. For example, unlike nearby dendritic shafts, the dendrite with invaginated filopodia-like structures exhibited an electron-dense cytoplasm with abundant mitochondria, SER and endosomal organelles, and received multiple Type 1 synapses (**Figure 9**). Three dendritic spines protruding from the shaft were reconstructed, with a presumptive fourth spine visible at the end of the volume (**Figure 8A**). Spines 1 and 2 each contained a spine apparatus and received a Type 1 synapse. Spine 3 also contained a spine apparatus, and was dually-innervated by a Type 1 and a Type 2 synapse. Together, these ultrastructural features indicate a neuronal region requiring greater energy production, calcium buffering and regulation, and secretory trafficking of integral membrane proteins to support enhanced synaptic neurotransmission[61].

Given the excellent ultrastructural preservation in the master volume, we performed a dense, 3D reconstruction of all neuronal and glial processes within a sub-volume for quantitative analysis of DLPFC layer 3 neuropil composition.

Quantitative Analysis of Densely-Reconstructed DLPFC Layer 3 Neuropil Sub-Volume.

Dense reconstruction of the sub-volume (**Figure 1D-E**) revealed the respective contributions of each type of neuronal and glial process (**Table 1**). Synaptic analysis showed greater density of Type 1 than Type 2 synapses, with an overall synaptic density of 0.39/μm^3. Axonal boutons forming Type 1 synapses preferentially targeted dendritic spines over shafts (**Table 2**). Of the 28 total axonal boutons identified in the sub-volume, 71% (n=20) formed a Type 1 synapse, 18% (n=5) formed a Type 2 synapse, and 11% (n=3) did not form a synapse. To further interrogate synaptic features of postmortem human DLPFC, we completed a targeted analysis of the predominant synaptic population-- Type 1 glutamatergic axo-spinous synapses.

Table 1. Proportion of neuronal and glial compartments present in the densely-reconstructed DLPFC layer 3 neuropil sub-volume

Cellular Compartment	Volume (μm^3)	% of total volume
Unmyelinated axons	19.1	29.7%
Dendritic shafts	15.6	24.3%
Astrocyte processes	9.3	14.4%
Axonal boutons	8.2	12.7%
Myelinated axons	3.0	4.7%
Dendritic spines	1.4	2.2%
Extracellular space	7.8	12.0%

Table 2. Synaptic bouton identity, density and postsynaptic target present in the densely-reconstructed DLPFC layer 3 neuropil sub-volume

Bouton Type	N	Density	Postsynaptic Target		
			Spine	Shaft	Axon
Synaptic- Type 1	20	0.31/μm^3	14 (70%)	6 (30%)	0
Synaptic- Type 2	5	0.08/μm^3	0	4 (80%)	1 (20%)
Non-synaptic	3	0.05/μm^3	--	--	--

Targeted Quantitative Analysis of Type 1 Synaptic, Sub-Synaptic and Organelle Structures.

A total of 50, Type 1 glutamatergic axo-spinous synapses were identified and reconstructed in 3D. Quantitative analysis (**Figure 10**) revealed the average sizes of synaptic axonal boutons (0.46 ± 0.26 μm^3), synaptic spines (0.15 ± 0.13 μm^3), presynaptic active zones (5.5 ± 3.8e^6 nm^3) and PSDs (8.0 ± 5.1e^6 nm^3). Mitochondria, identified in 52% (n=26) of Type 1 synaptic boutons, had an average volume of 0.09 ± 0.05 μm^3. All bouton mitochondria exhibited globular morphology (mean aspect ratio = 0.99). Of the synaptic spines, 88% (n=44) contained a spine apparatus. Because these core synaptic components were sufficiently preserved for quantitative volumetric and morphologic analysis, we next sought to determine whether the within- and trans-synaptic structure relationships that reflect functional synaptic communication were maintained postmortem.

Targeted Quantitative Analysis of Type 1 Pre- and Postsynaptic Structure Relationships

Presynaptic bouton and active zone volumes were positively correlated (r=0.60, p=4.0e^{-6}; **Figure 11A**), as were spine and PSD volumes (r=0.43, p=0.002; **Figure 11B**). Analyses of trans-synaptic structures revealed positive correlations between presynaptic bouton and postsynaptic spine volumes (r=0.37, p=0.008; **Figure 11C**) and presynaptic active zone and PSD volumes (r=0.76, p=1.2e^{-10}; **Figure 11D**). To further evaluate whether trans-synaptic ultrastructural relationships persist in the postmortem human brain, we compared synapses based on the presence of mitochondria or a spine apparatus, two organelles indicative of greater synaptic function and activity. Type 1 axo-spinous synapses with presynaptic mitochondria had significantly greater bouton, active zone and PSD volumes, and were significantly more likely to target a spine with a spine apparatus (**Table 3**). Type 1 axo-spinous synapses with a postsynaptic spine apparatus had significantly greater mean spine, active zone and PSD volumes (**Table 4**). These convergent results support that the fundamental ultrastructural features reflecting synaptic function and activity observed in model organisms are preserved in postmortem human DLPFC.

Table 3. Comparison of synaptic, sub-synaptic and mitochondrial volumes based on mitochondrion abundance in Type 1 axo-spinous synapses.

Measure	# Mitochondria in synaptic axonal boutons				Statistic*
	0	1	2	3	
# Boutons	24	22	3	1	--
Mitochondria Volume μm^3	--	0.10 ± 0.04	0.11 ± 0.07	0.04 ± 0.01	--
Bouton volume μm^3	0.27 ± 0.14	0.51 ± 0.19	0.57 ± 0.08	0.21	$F_{1,48}$=24.8 p=9.0e^{-6}
Spine volume μm^3	0.12 ± 0.15	0.14 ± 0.09	0.17 ± 0.02	0.16	$F_{1,48}$=0.74 p=0.4
Active Zone volume nm^3	3.76 ± 2.60e^6	6.63 ± 4.23e^6	1.01 ± 3.38e^7	6.80e^6	$F_{1,48}$=11.07 p=0.002
PSD volume nm^3	5.76 ± 4.16e^6	9.24 ± 4.20e^6	1.57 ± 3.38e^7	1.38 e^7	$F_{1,48}$=11.02 p=0.002
% Spines with an Apparatus	33%	90%	100%	100%	χ^2 = 11.0 p = 0.0009

Values are counts or mean ± standard deviation. *For statistical comparisons, the independent measure was presence or absence of mitochondria in axonal boutons.

Table 4. Comparison of synaptic, sub-synaptic and mitochondrial volumes in Type 1 axo-spinous synapses based on presence of a spine apparatus.

Measure	Spine Apparatus		Statistic
	Yes	No	
# Spines	44	6	--
Bouton volume μm^3	0.41 ± 0.21	0.24 ± 0.11	$F_{1,48}$=3.72, p=0.06
Spine volume μm^3	0.15 ± 0.12	0.04 ± 0.03	$F_{1,48}$=4.47, p=0.04
Active Zone volume nm^3	5.91 ± 3.87e^6	2.25 ± 0.89e^6	$F_{1,48}$=5.22, p=0.03
PSD volume nm^3	8.61 ± 5.14e^6	3.45 ± 1.84e^6	$F_{1,48}$=6.01, p=0.02
% Boutons containing mitochondria	57%	17%	χ^2 = 3.4 p = 0.06
Mitochondria volume μm^3	0.11 ± 0.06	0.10	$F_{1,48}$=0.005, p=0.9

Values are counts or mean ± standard deviation.

DISCUSSION

We employed an advanced VEM imaging tool, FIB-SEM, to determine if ultrastructural correlates of *in vivo* glutamate synapse function and activity are preserved *ex vivo* in the postmortem human brain. To address this goal, we first optimized a workflow to generate postmortem human DLPFC tissue samples with the ultrastructural preservation and enhanced-contrast staining required for FIB-SEM imaging. Second, we successfully imaged a volume (2,630 mm^3) of DLPFC layer 3 with a 5nm mill step-size via FIB-SEM, ensuring

little to no loss of information. Third, we implemented a semi-automated data collection approach to complete a dense 3D reconstruction of a sub-volume of postmortem human DLPFC layer 3. Finally, we used this semi-automated approach to reconstruct sub-cellular, sub-synaptic and mitochondrial components within 50 glutamate axo-spinous synapses. Quantitative analysis of these 3D datasets revealed that ultrastructural features of synaptic function and activity were preserved within and across individual synapses in postmortem human brain tissue. Thus, our findings provide proof-of-concept that *in vivo* functioning of individual synapses in human brain can be investigated *ex vivo* in tissue obtained postmortem and analyzed by FIB-SEM.

DLPFC layer 3 neuropil organization was revealed by dense reconstruction and quantitative analysis. The relative proportion of DLPFC layer 3 neuropil occupied by each type of cellular compartment was remarkably similar to recent VEM findings in biopsy-obtained temporal cortex layer 3[80], as was the volumetric proportion reflecting extracellular space in biopsy-obtained prefrontal cortex[78]. The mean synaptic density observed by VEM imaging of biopsy cortical samples[79-84] ranges from 0.0002/mm^3 – 0.74/mm^3, and of autopsy cortical samples[81,85-89] from 0.40/mm^3 – 0.76/mm^3. Our current finding of 0.39/mm^3 in DLPFC layer 3 is consistent with these existing data, which span multiple cortical areas and layers, and is also consistent with previous findings in monkey DLPFC layer 3[90]. In our dense reconstruction, 80% of identified synapses were Type 1 and the remaining 20% were Type 2. These proportions are highly consistent with findings in layer 3 of biopsied temporal cortex 3[80], but lower than the findings of 92-95% Type 1 synapses in postmortem temporal cortex layers 2 – 5[81,85-89] and anterior cingulate cortex layer 3[85]. Findings regarding the effects of PMI on Type 1 and 2 synapse identification are highly mixed (for review see[91]). Some evidence suggests that PSD size may increase with PMI[92], resulting in the possible mis-identification of Type 2 synapses as Type 1. However, our findings indicate this potential confound was likely not present, and/or the rich, 3D ultrastructural data available for every synaptic contact mitigated any PMI effect on synapse identification. Finally, our finding that 70% of Type 1 synapses were formed onto dendritic spines is consistent with previous VEM studies of biopsy[79,83,84] and autopsy[81,85-87] cortical samples which found, respectively, that 82-90% and 55-73% of Type 1 synapses were formed onto dendritic spines. Thus, all neuropil components, including Type 1 and Type 2 synapses, were identifiable and quantifiable via FIB-SEM imaging using the tissue processing workflow optimized for postmortem human brain.

Targeted 3D ultrastructural analysis of Type 1 axo-spinous glutamatergic synapses similarly demonstrated that synaptic nanoarchitecture is preserved in postmortem human DLPFC. For example, in the

normal brain, active zone and PSD sizes are highly correlated, which reflects that pre- and postsynaptic components must act together as a functional unit for effective synaptic communication[34,35]. Active zone and PSD sizes are also diverse in the normal brain, which reflects the dynamic range of synaptic activity and plasticity contributing to complex neural computation[93-95]. Both of these core synaptic features were clearly evident in postmortem human DLPFC, suggesting that the synaptic functional unit remained intact postmortem.

Analysis of mitochondria and spine apparatuses, synaptic organelles who presence is indicative of greater activity and neurotransmission, further demonstrated preserved glutamatergic synaptic relationships within postmortem DLPFC. For example, mitochondria are trafficked to more active synaptic boutons, providing the required energetic support for efficient neurotransmitter release[65,96]. Similarly, spine apparatuses are present in dendritic spines that are more synaptically active, enhancing postsynaptic Ca^{2+} buffering and post-translational modification capabilities[69,70]. Consistent with these findings from model organisms, Type 1 axo-spinous synapses with presynaptic mitochondria had significantly greater mean active zone and PSD volumes, and significantly more of these synapses contained a spine apparatus. Likewise, glutamatergic synapses with a postsynaptic spine apparatus had significantly greater mean active zone and PSD volumes, and significantly more of these synapses contained presynaptic mitochondria. Together, the synaptic nanoarchitecture and organelle findings provide convergent support that relative *in vivo* synaptic function and activity can be interrogated *ex vivo* in postmortem human brain tissue via quantitative FIB-SEM imaging and analysis.

In the DLPFC layer 3 neuropil volume, we reconstructed a spiny dendritic shaft that exhibited unique and complex ultrastructural features characteristic of heightened synaptic communication, integration and plasticity. Unlike nearby shafts, which exhibited typical dendritic ultrastructure[57], this dendritic segment had an electron-dense cytoplasm and an abundance of mitochondria and single-membrane organelles, such as SER and endosomes. Furthermore, we also identified four discrete sub-cellular processes situated within this dendrite's cytoplasm. These invaginating sub-cellular structures and the surrounding dendritic cytoplasm had distinct membranes[97], which exhibited multiple sites of contact resembling non-synaptic puncta adhaerens[57]. Unexpectedly, these invaginating processes were not connected to any parent structure, instead presenting as independent entities within the dendritic shaft. Such a relationship suggests these structures, which resemble dendritic or axonal filopodia[76], were trans-endocytosed by the parent dendrite[77]. Invaginating structures are implicated in synaptic formation, maintenance, pruning and plasticity, and provide a unique means to further

enhance the functional flexibility of the invaginated structure[76,77,97-100]. Thus, this dendritic segment appears to be a hub of substantial postsynaptic resources that enhance the capacity for localized synaptic integration and computation[101,102]. A dendritic segment exhibiting these features has not been reported in either human or non-human cortex to our knowledge. The PFC is a region uniquely expanded in humans[103], and exhibits molecular and cytoarchitectonic features thought to underlie many higher-order functions specific to humans[104]. Indeed, the uniqueness of human PFC may contribute to the apparent human-specificity of serious brain disorders[105] such as schizophrenia[43], autism spectrum disorder[42] and Alzheimer's disease[106]. Future comparative VEM studies of DLPFC neuropil will provide valuable insight into the exceptional nature of human brain.

In sum, the current findings provide proof-of-concept evidence that *in vivo* functioning of individual synapses in human brain can be investigated *ex vivo* in tissue obtained postmortem and analyzed by VEM. Our tissue processing workflow generated 3D datasets of excellent fixation, staining and ultrastructural preservation using samples with a PMI of 6.0 hours and that were in storage for more than 8 years before staining and FIB-SEM imaging. The success of this approach is consistent both with existing EM data demonstrating that ultrastructure is preserved, and light microscopic data of synaptic appositions, in postmortem human samples of longer PMIs (for examples, see[46,48,54,107,108]). The suitability of both biopsy and autopsy human brain tissue samples, and of archived tissue samples, for quantitative VEM greatly expands the potential resource pool and opportunities to investigate ultrastructural correlates of neural function in human health and disease. These findings show that not only are these sub-synaptic structures able to be identified, segmented and reconstructed in 3D in postmortem human brain, but that the biological processes occurring postmortem do not affect fundamental pre- and postsynaptic relationships. Finally, our use of FIB-SEM technology has revealed a potentially novel and hub-like dendritic organization in human DLPFC. Together, these findings indicate that VEM imaging studies of postmortem human brain can be used to investigate the nature of synaptic dysfunction in severe brain disorders, such as schizophrenia and autism spectrum disorder.

ACKNOWLEDGEMENTS

The authors gratefully acknowledge the digital graphics expertise of Mary Brady. Funding support was provided by NIH grants R01MH132544 (JRG), S10MH133575 (JRG, ZF), R01ES034037 (ZF), R21AA028800 (ZF),

Commonwealth of Pennsylvania Formula Fund (ZF), The Pittsburgh Foundation (ZF), and Baszucki Brain Research Funds (ZF).

CONFLICT OF INTEREST

David A. Lewis currently receives investigator-initiated research support from Merck.

BIBLIOGRAPHY

1 Ho, V. M., Lee, J.-A. & Martin, K. C. The cell biology of synaptic plasticity. *Science* **334**, 623-628 (2011).

2 Glausier, J. R. & Lewis, D. A. Mapping pathologic circuitry in schizophrenia. *Handb. Clin. Neurol.* **150**, 389-417 (2018).

3 Howes, O. D. & Onwordi, E. C. The synaptic hypothesis of schizophrenia version III: a master mechanism. *Mol. Psychiatry* (2023).

4 Neniskyte, U. & Gross, C. T. Errant gardeners: glial-cell-dependent synaptic pruning and neurodevelopmental disorders. *Nature Reviews Neuroscience* **18**, 658-670 (2017).

5 Heuser , J. E. & Reese , T. S. EVIDENCE FOR RECYCLING OF SYNAPTIC VESICLE MEMBRANE DURING TRANSMITTER RELEASE AT THE FROG NEUROMUSCULAR JUNCTION. *J. Cell Biol.* **57**, 315-344 (1973).

6 Palay, S. L. in *Brain Function: RNA and Brain Function, Memory and Learning* Vol. II (ed M. A. B. Brazier) 69-100 (University of California Press, 1964).

7 Holler, S., Köstinger, G., Martin, K. A. C., Schuhknecht, G. F. P. & Stratford, K. J. Structure and function of a neocortical synapse. *Nature* **591**, 111-116 (2021).

8 Schikorski, T. & Stevens, C. F. Quantitative Ultrastructural Analysis of Hippocampal Excitatory Synapses. *The Journal of Neuroscience* **17**, 5858-5867 (1997).

9 Matz, J., Gilyan, A., Kolar, A., McCarvill, T. & Krueger, S. R. Rapid structural alterations of the active zone lead to sustained changes in neurotransmitter release. *Proc. Natl. Acad. Sci. U. S. A.* **107**, 8836-8841 (2010).

10 Maschi, D. & Klyachko, V. A. Spatiotemporal Regulation of Synaptic Vesicle Fusion Sites in Central Synapses. *Neuron* **94**, 65-73.e63 (2017).

11 Südhof, T. C. The presynaptic active zone. *Neuron* **75**, 11-25 (2012).

12 Takumi, Y., Ramírez-León, V., Laake, P., Rinvik, E. & Ottersen, O. P. Different modes of expression of AMPA and NMDA receptors in hippocampal synapses. *Nat. Neurosci.* **2**, 618-624 (1999).

13 Shinohara, Y. *et al.* Left-right asymmetry of the hippocampal synapses with differential subunit allocation of glutamate receptors. *Proc. Natl. Acad. Sci. U. S. A.* **105**, 19498-19503 (2008).

14 Fukazawa, Y. & Shigemoto, R. Intra-synapse-type and inter-synapse-type relationships between synaptic size and AMPAR expression. *Curr. Opin. Neurobiol.* **22**, 446-452 (2012).

15 Chen, X. *et al.* PSD-95 family MAGUKs are essential for anchoring AMPA and NMDA receptor complexes at the postsynaptic density. *Proceedings of the National Academy of Sciences* **112**, E6983-E6992 (2015).

16 Patriarchi, T., Buonarati, O. R. & Hell, J. W. Postsynaptic localization and regulation of AMPA receptors and Cav1.2 by β2 adrenergic receptor/PKA and Ca(2+)/CaMKII signaling. *EMBO J.* **37** (2018).

17 Rangaraju, V., Calloway, N. & Ryan, T. A. Activity-driven local ATP synthesis is required for synaptic function. *Cell* **156**, 825-835 (2014).

18 Ivannikov, M. V., Sugimori, M. & Llinás, R. R. Synaptic vesicle exocytosis in hippocampal synaptosomes correlates directly with total mitochondrial volume. *J. Mol. Neurosci.* **49**, 223-230 (2013).

19 Attwell, D. & Laughlin, S. B. An energy budget for signaling in the grey matter of the brain. *J. Cereb. Blood Flow Metab.* **21**, 1133-1145 (2001).

20 Hall, C. N., Klein-Flugge, M. C., Howarth, C. & Attwell, D. Oxidative phosphorylation, not glycolysis, powers presynaptic and postsynaptic mechanisms underlying brain information processing. *J. Neurosci.* **32**, 8940-8951 (2012).

21 Harris, J. J., Jolivet, R. & Attwell, D. Synaptic energy use and supply. *Neuron* **75**, 762-777 (2012).

22 Howarth, C., Gleeson, P. & Attwell, D. Updated energy budgets for neural computation in the neocortex and cerebellum. *J. Cereb. Blood Flow Metab.* **32**, 1222-1232 (2012).

23 Ma, H., Cai, Q., Lu, W., Sheng, Z. H. & Mochida, S. KIF5B motor adaptor syntabulin maintains synaptic transmission in sympathetic neurons. *J. Neurosci.* **29**, 13019-13029 (2009).

24 Verstreken, P. *et al.* Synaptic mitochondria are critical for mobilization of reserve pool vesicles at Drosophila neuromuscular junctions. *Neuron* **47**, 365-378 (2005).

25 Li, S., Xiong, G. J., Huang, N. & Sheng, Z. H. The cross-talk of energy sensing and mitochondrial anchoring sustains synaptic efficacy by maintaining presynaptic metabolism. *Nat Metab* **2**, 1077-1095 (2020).

26 Seager, R., Lee, L., Henley, J. M. & Wilkinson, K. A. Mechanisms and roles of mitochondrial localisation and dynamics in neuronal function. *Neuronal Signal* **4**, Ns20200008 (2020).

27 Justs, K. A. *et al.* Presynaptic Mitochondrial Volume and Packing Density Scale with Presynaptic Power Demand. *The Journal of Neuroscience* **42**, 954-967 (2022).
28 Li, S. & Sheng, Z. H. Energy matters: presynaptic metabolism and the maintenance of synaptic transmission. *Nat. Rev. Neurosci.* (2021).
29 Rossi, M. J. & Pekkurnaz, G. Powerhouse of the mind: mitochondrial plasticity at the synapse. *Curr. Opin. Neurobiol.* **57**, 149-155 (2019).
30 Mendelsohn, R. *et al.* Morphological principles of neuronal mitochondria. *J. Comp. Neurol.* **530**, 886-902 (2022).
31 Hackenbrock, C. R. Energy-linked condensed-orthodox ultrastructural transformations in mitochondria. *Chemotherapy* **27 Suppl 2**, 21-26 (1981).
32 Scalettar, B. A., Abney, J. R. & Hackenbrock, C. R. Dynamics, structure, and function are coupled in the mitochondrial matrix. *Proc Natl Acad Sci U.S.A* **88**, 8057-8061 (1991).
33 Cserép, C., Pósfai, B., Schwarcz, A. D. & Dénes, Á. Mitochondrial Ultrastructure Is Coupled to Synaptic Performance at Axonal Release Sites. *eneuro* **5**, ENEURO.0390-0317.2018 (2018).
34 Südhof, T. C. & Malenka, R. C. Understanding synapses: past, present, and future. *Neuron* **60**, 469-476 (2008).
35 Di Maio, V. The glutamatergic synapse: a complex machinery for information processing. *Cogn. Neurodyn.* **15**, 757-781 (2021).
36 Sanderson, T. M., Georgiou, J. & Collingridge, G. L. Illuminating Relationships Between the Pre- and Post-synapse. *Front Neural Circuits* **14**, 9 (2020).
37 Smith, H. L. *et al.* Mitochondrial support of persistent presynaptic vesicle mobilization with age-dependent synaptic growth after LTP. *Elife* **5** (2016).
38 Miller, E. K. & Cohen, J. D. An integrative theory of prefrontal cortex function. *Annu. Rev. Neurosci.* **24**, 167-202 (2001).
39 Fuster, J. M. The prefrontal cortex - an update: Time is of the essence. *Neuron* **30**, 319-333 (2001).
40 Donahue, C. J., Glasser, M. F., Preuss, T. M., Rilling, J. K. & Van Essen, D. C. Quantitative assessment of prefrontal cortex in humans relative to nonhuman primates. *Proc. Natl. Acad. Sci. U. S. A.* **115**, E5183-e5192 (2018).
41 Spocter, M. A. *et al.* Neuropil distribution in the cerebral cortex differs between humans and chimpanzees. *J. Comp. Neurol.* **520**, 2917-2929 (2012).
42 Liu, X. *et al.* Disruption of an Evolutionarily Novel Synaptic Expression Pattern in Autism. *PLoS Biol.* **14**, e1002558 (2016).
43 Ogawa, L. M. & Vallender, E. J. Evolutionary conservation in genes underlying human psychiatric disorders. *Front. Hum. Neurosci.* **8**, 283 (2014).
44 Levchenko, A., Gusev, F. & Rogaev, E. The evolutionary origin of psychosis. *Frontiers in psychiatry* **14** (2023).
45 Teffer, K. & Semendeferi, K. in *Prog. Brain Res.* Vol. 195 (eds Michel A. Hofman & Dean Falk) 191-218 (Elsevier, 2012).
46 Glausier, J. R. *et al.* Laminar Differences in the Targeting of Dendritic Spines by Cortical Pyramidal Neurons and Interneurons in Human Dorsolateral Prefrontal Cortex. *Neuroscience* **452**, 181-191 (2021).
47 Rees, S. A quantitative electron microscopic study of the ageing human cerebral cortex. *Acta Neuropathol.* **36**, 347-362 (1976).
48 Glausier, J. R., Konanur, A. & Lewis, D. A. Factors Affecting Ultrastructural Quality in the Prefrontal Cortex of the Postmortem Human Brain. *J. Histochem. Cytochem.* **67**, 185-202 (2019).
49 Glausier, J. R., Roberts, R. C. & Lewis, D. A. Ultrastructural analysis of parvalbumin synapses in human dorsolateral prefrontal cortex. *J. Comp. Neurol.* **525**, 2075-2089 (2017).
50 Kuwajima, M., Spacek, J. & Harris, K. M. Beyond counts and shapes: studying pathology of dendritic spines in the context of the surrounding neuropil through serial section electron microscopy. *Neuroscience* **251**, 75-89 (2013).
51 Peddie, C. J. *et al.* Volume electron microscopy. *Nature Reviews Methods Primers* **2**, 51 (2022).
52 Glantz, L. A. & Lewis, D. A. Decreased dendritic spine density on prefrontal cortical pyramidal neurons in schizophrenia. *Arch. Gen. Psychiatry* **57**, 65-73 (2000).
53 Glausier, J. R., Kelly, M. A., Salem, S., Chen, K. & Lewis, D. A. Proxy measures of premortem cognitive aptitude in postmortem subjects with schizophrenia. *Psychol Med* **50**, 507-514 (2020).
54 Glausier, J. R., Fish, K. N. & Lewis, D. A. Altered parvalbumin basket cell inputs in the dorsolateral prefrontal cortex of schizophrenia subjects. *Mol. Psychiatry* **19**, 30-36 (2014).

55 Hua, Y., Laserstein, P. & Helmstaedter, M. Large-volume en-bloc staining for electron microscopy-based connectomics. *Nature communications* **6**, 7923 (2015).
56 Gray, E. G. Axo-somatic and axo-dendritic synapses of the cerebral cortex: An electron microscopic study. *J. Anat.* **93**, 420-433 (1959).
57 Peters, A., Palay, S. L. & Webster, D. F. *The Fine Structure of The Nervous System*. Vol. 3 (Oxford University Press, 1991).
58 Colonnier, M. in *The Organization of the Cerebral Cortex* (eds F. O. Schmidt, F. G. Worden, G. Adelman, & S. G. Dennis) 125-152 (MIT Press, 1981).
59 Merchán-Pérez, A., Rodriguez, J. R., Alonso-Nanclares, L., Schertel, A. & Defelipe, J. Counting Synapses Using FIB/SEM Microscopy: A True Revolution for Ultrastructural Volume Reconstruction. *Front. Neuroanat.* **3**, 18 (2009).
60 Peters, A. & Jones, E. G. Vol. 1 565 (Plenum Press, 1984).
61 Harris, K. M. & Weinberg, R. J. Ultrastructure of synapses in the mammalian brain. *Cold Spring Harb. Perspect. Biol.* **4** (2012).
62 Akert, K., Moor, H. & Pfenninger, K. Synaptic fine structure. *Adv. Cytopharmacol.* **1**, 273-290 (1971).
63 Perkins, G. *et al.* Electron Tomography of Neuronal Mitochondria: Three-Dimensional Structure and Organization of Cristae and Membrane Contacts. *J. Struct. Biol.* **119**, 260-272 (1997).
64 Glancy, B., Kim, Y., Katti, P. & Willingham, T. B. The Functional Impact of Mitochondrial Structure Across Subcellular Scales. *Front. Physiol.* **11**, 541040 (2020).
65 Devine, M. J. & Kittler, J. T. Mitochondria at the neuronal presynapse in health and disease. *Nat. Rev. Neurosci.* **19**, 63-80 (2018).
66 Hara, Y. *et al.* Presynaptic mitochondrial morphology in monkey prefrontal cortex correlates with working memory and is improved with estrogen treatment. *Proc. Natl. Acad. Sci. U. S. A.* **111**, 486-491 (2014).
67 Liu, X. & Hajnóczky, G. Altered fusion dynamics underlie unique morphological changes in mitochondria during hypoxia-reoxygenation stress. *Cell Death Differ.* **18**, 1561-1572 (2011).
68 Ahmad, T. *et al.* Computational classification of mitochondrial shapes reflects stress and redox state. *Cell Death Dis.* **4**, e461 (2013).
69 Perez-Alvarez, A. *et al.* Endoplasmic reticulum visits highly active spines and prevents runaway potentiation of synapses. *Nature communications* **11**, 5083 (2020).
70 Chirillo, M. A., Waters, M. S., Lindsey, L. F., Bourne, J. N. & Harris, K. M. Local resources of polyribosomes and SER promote synapse enlargement and spine clustering after long-term potentiation in adult rat hippocampus. *Sci. Rep.* **9**, 3861 (2019).
71 Spacek, J. & Harris, K. M. Three-Dimensional Organization of Smooth Endoplasmic Reticulum in Hippocampal CA1 Dendrites and Dendritic Spines of the Immature and Mature Rat. *The Journal of Neuroscience* **17**, 190-203 (1997).
72 Parker, P., Kuwajima, M. & Harris, K. M. *SER and Spine Apparatus Identification*, <https://synapseweb.clm.utexas.edu/> (2019).
73 Melchitzky, D. S., Sesack, S. R., Pucak, M. L. & Lewis, D. A. Synaptic targets of pyramidal neurons providing intrinsic horizontal connections in monkey prefrontal cortex. *The Journal of Comparative Neurology* **390**, 211-224 (1998).
74 Pucak, M. L., Levitt, J. B., Lund, J. S. & Lewis, D. A. Patterns of intrinsic and associational circuitry in monkey prefrontal cortex. *The Journal of Comparative Neurology* **376**, 614-630 (1996).
75 Levitt, J. B., Lewis, D. A., Yoshioka, T. & Lund, J. S. Topography of pyramidal neuron intrinsic connections in macaque monkey prefrontal cortex (areas 9 and 46). *J. Comp. Neurol.* **338**, 360-376 (1993).
76 Fiala, J. C., Feinberg, M., Popov, V. & Harris, K. M. Synaptogenesis via dendritic filopodia in developing hippocampal area CA1. *J. Neurosci.* **18**, 8900-8911 (1998).
77 Spacek, J. & Harris, K. M. Trans-endocytosis via spinules in adult rat hippocampus. *J. Neurosci.* **24**, 4233-4241 (2004).
78 Karlupia, N. *et al.* Immersion Fixation and Staining of Multicubic Millimeter Volumes for Electron Microscopy-Based Connectomics of Human Brain Biopsies. *Biol. Psychiatry* **94**, 352-360 (2023).
79 Rollenhagen, A. *et al.* Synaptic Organization of the Human Temporal Lobe Neocortex as Revealed by High-Resolution Transmission, Focused Ion Beam Scanning, and Electron Microscopic Tomography. *Int. J. Mol. Sci.* **21** (2020).
80 Shapson-Coe, A. *et al.* A connectomic study of a petascale fragment of human cerebral cortex. *bioRxiv*, 2021.2005.2029.446289 (2021).

81 Cano-Astorga, N., DeFelipe, J. & Alonso-Nanclares, L. Three-Dimensional Synaptic Organization of Layer III of the Human Temporal Neocortex. *Cereb. Cortex* **31**, 4742-4764 (2021).
82 Schmuhl-Giesen, S. *et al.* Sublamina-Specific Dynamics and Ultrastructural Heterogeneity of Layer 6 Excitatory Synaptic Boutons in the Adult Human Temporal Lobe Neocortex. *Cereb. Cortex* **32**, 1840-1865 (2022).
83 Yakoubi, R. *et al.* Ultrastructural heterogeneity of layer 4 excitatory synaptic boutons in the adult human temporal lobe neocortex. *Elife* **8** (2019).
84 Yakoubi, R. *et al.* Quantitative Three-Dimensional Reconstructions of Excitatory Synaptic Boutons in Layer 5 of the Adult Human Temporal Lobe Neocortex: A Fine-Scale Electron Microscopic Analysis. *Cereb. Cortex* **29**, 2797-2814 (2019).
85 Cano-Astorga, N., Plaza-Alonso, S., DeFelipe, J. & Alonso-Nanclares, L. 3D synaptic organization of layer III of the human anterior cingulate and temporopolar cortex. *Cereb. Cortex* (2023).
86 Domínguez-Álvaro, M., Montero-Crespo, M., Blazquez-Llorca, L., DeFelipe, J. & Alonso-Nanclares, L. 3D Electron Microscopy Study of Synaptic Organization of the Normal Human Transentorhinal Cortex and Its Possible Alterations in Alzheimer's Disease. *eNeuro* **6** (2019).
87 Domínguez-Álvaro, M., Montero-Crespo, M., Blazquez-Llorca, L., DeFelipe, J. & Alonso-Nanclares, L. 3D Ultrastructural Study of Synapses in the Human Entorhinal Cortex. *Cereb. Cortex* **31**, 410-425 (2021).
88 Domínguez-Álvaro, M. *et al.* Three-dimensional analysis of synapses in the transentorhinal cortex of Alzheimer's disease patients. *Acta neuropathologica communications* **6**, 20 (2018).
89 Domínguez-Álvaro, M. *et al.* 3D Analysis of the Synaptic Organization in the Entorhinal Cortex in Alzheimer's Disease. *eNeuro* **8** (2021).
90 Dumitriu, D. *et al.* Selective changes in thin spine density and morphology in monkey prefrontal cortex correlate with aging-related cognitive impairment. *J. Neurosci.* **30**, 7507-7515 (2010).
91 Krassner, M. M. *et al.* Postmortem changes in brain cell structure: a review. *Free Neuropathol* **4** (2023).
92 Roberts, R. C., Gaither, L. A., Peretti, F. J., Lapidus, B. & Chute, D. J. Synaptic organization of the human striatum: a postmortem ultrastructural study. *J. Comp. Neurol.* **374**, 523-534 (1996).
93 Atwood, H. L. & Karunanithi, S. Diversification of synaptic strength: presynaptic elements. *Nature Reviews Neuroscience* **3**, 497-516 (2002).
94 Abbott, L. F. & Regehr, W. G. Synaptic computation. *Nature* **431**, 796-803 (2004).
95 Scholl, B. & Fitzpatrick, D. Cortical synaptic architecture supports flexible sensory computations. *Curr. Opin. Neurobiol.* **64**, 41-45 (2020).
96 MacAskill, A. F., Atkin, T. A. & Kittler, J. T. Mitochondrial trafficking and the provision of energy and calcium buffering at excitatory synapses. *Eur. J. Neurosci.* **32**, 231-240 (2010).
97 Petralia, R. S., Yao, P. J., Kapogiannis, D. & Wang, Y. X. Invaginating Structures in Synapses - Perspective. *Front. Synaptic Neurosci.* **13**, 685052 (2021).
98 Petralia, R. S., Wang, Y. X., Mattson, M. P. & Yao, P. J. Invaginating Structures in Mammalian Synapses. *Front. Synaptic Neurosci.* **10**, 4 (2018).
99 Campbell, C., Lindhartsen, S., Knyaz, A., Erisir, A. & Nahmani, M. Cortical Presynaptic Boutons Progressively Engulf Spinules as They Mature. *eNeuro* **7** (2020).
100 Zaccard, C. R., Gippo, I., Song, A., Geula, C. & Penzes, P. Dendritic spinule-mediated structural synaptic plasticity: Implications for development, aging, and psychiatric disease. *Front. Mol. Neurosci.* **16**, 1059730 (2023).
101 Lafourcade, M. *et al.* Differential dendritic integration of long-range inputs in association cortex via subcellular changes in synaptic AMPA-to-NMDA receptor ratio. *Neuron* **110**, 1532-1546.e1534 (2022).
102 Fischer, L. *et al.* Dendritic Mechanisms for In Vivo Neural Computations and Behavior. *J. Neurosci.* **42**, 8460-8467 (2022).
103 Preuss, T. M. The human brain: rewired and running hot. *Ann. N. Y. Acad. Sci.* **1225 Suppl 1**, E182-191 (2011).
104 Kolk, S. M. & Rakic, P. Development of prefrontal cortex. *Neuropsychopharmacology* **47**, 41-57 (2022).
105 Vanderhaeghen, P. & Polleux, F. Developmental mechanisms underlying the evolution of human cortical circuits. *Nat. Rev. Neurosci.* **24**, 213-232 (2023).
106 Rosen, R. F. *et al.* Comparative pathobiology of beta-amyloid and the unique susceptibility of humans to Alzheimer's disease. *Neurobiol. Aging* **44**, 185-196 (2016).
107 Kay, K. R. *et al.* Studying synapses in human brain with array tomography and electron microscopy. *Nat. Protoc.* **8**, 1366-1380 (2013).

108 Sele, M. *et al.* Optimization of ultrastructural preservation of human brain for transmission electron microscopy after long post-mortem intervals. *Acta neuropathologica communications* **7**, 144 (2019).

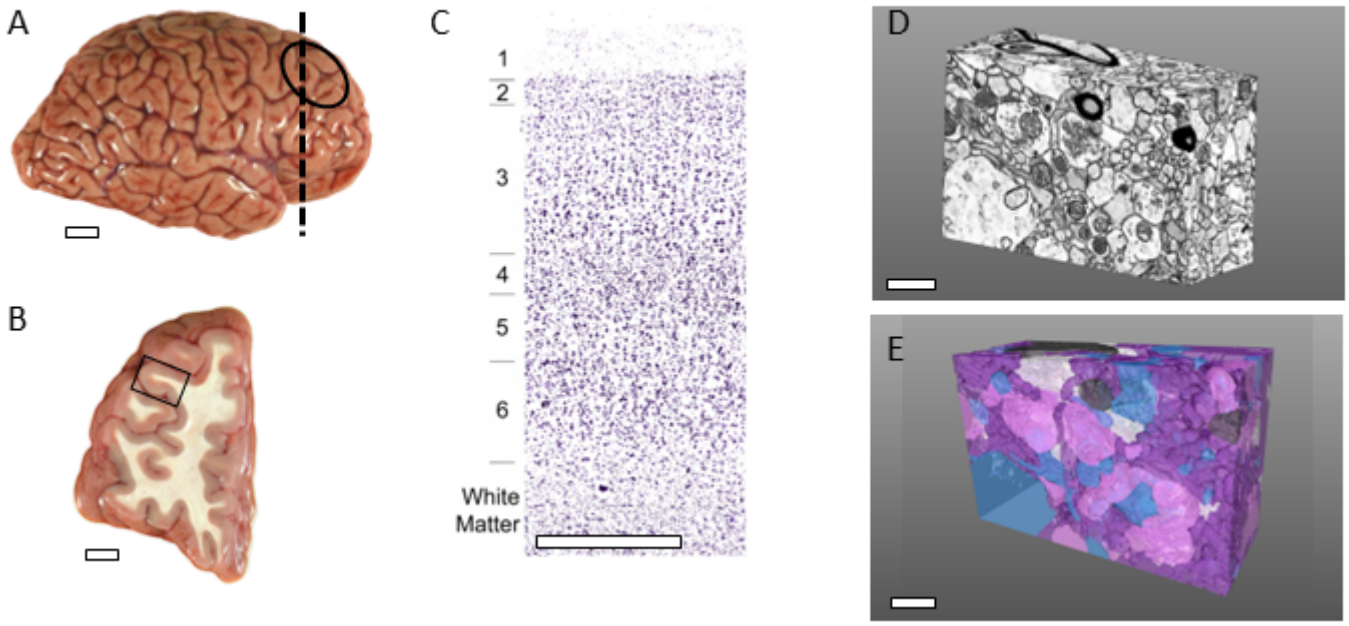

Figure 1. Overview of postmortem human brain tissue sampling and 3D reconstruction. A) Lateral view of postmortem human brain hemisphere. Circle shows the approximate location of the DLPFC region. **B)** Coronal view of the DLPFC at the approximate rostro-caudal level indicated by the vertical dashed line in A. Box indicates the approximate region sampled for this study. **C)** Nissl-stained tissue section from the approximate location shown by the box in B. Cortical layers are numbered, and tissue was sampled from layer 3 for the current study. **D)** Postmortem human DLPFC layer 3 neuropil volume imaged in 3D via FIB-SEM. **E)** Corresponding dense 3D reconstruction of neuronal and glial profiles shown in D. Glutamate axonal boutons (pink), dendritic shafts and spines (blue), un-myelinated axons (purple), myelinated axons (dark grey), and astrocytic processes (white). Scale bar in A is 2 cm, B is 1 cm, C is 1 mm, and D and E are 1 μm.

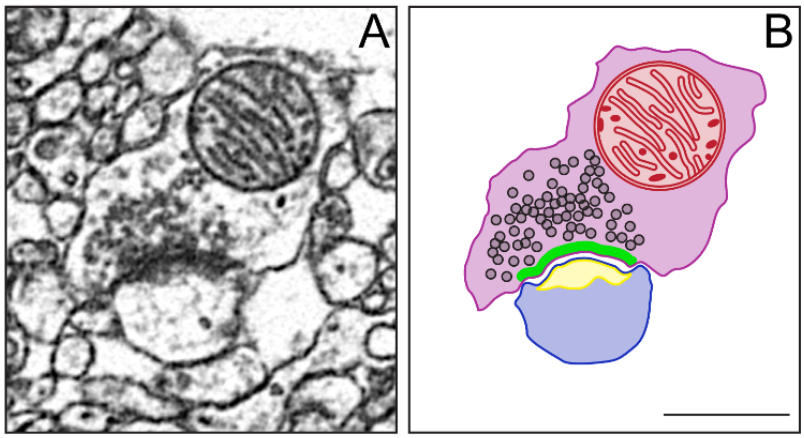

Figure 2. Glutamatergic synaptic structure. A) Single SEM image illustrating the defining ultrastructural features of a Type 1 glutamate synapse. Micrograph captured via FIB-SEM VEM imaging of human DLPFC layer 3. **B)** Illustration of the synapse shown in panel A. The glutamate axonal bouton (pink) containing synaptic vesicles (brown), a mitochondrion (red) and an active zone (green) forms an asymmetric synapse identified by the prominent PSD (yellow) onto a dendritic spine (blue). Scale bar is 630 nm in A and B.

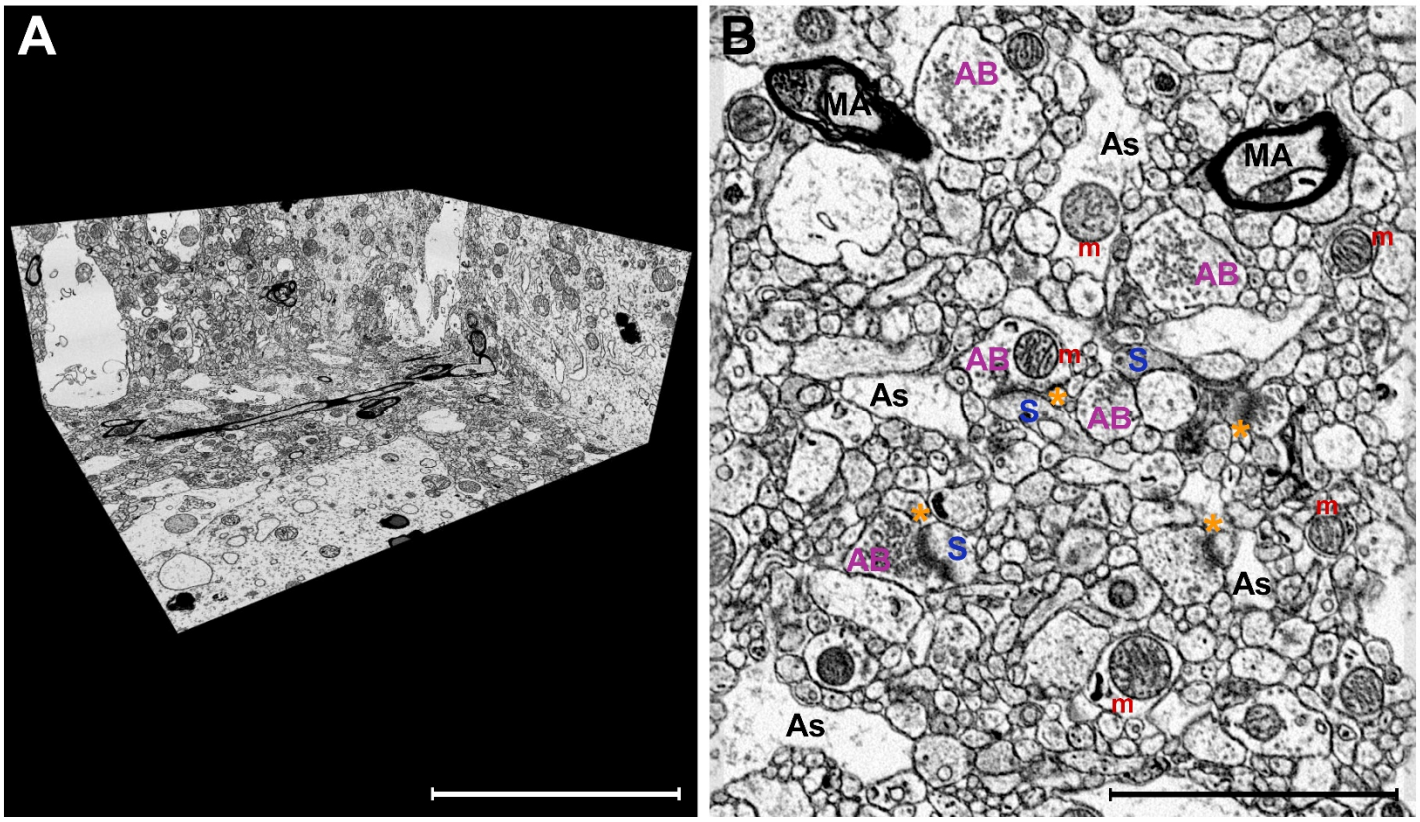

Figure 3. Excellent ultrastructural preservation of postmortem human brain tissue processed for FIB-SEM imaging. A) A perspective overview of a volume of DLPFC layer 3 captured with a voxel size of 5x5x5 nm. **B)** A representative SEM image using in-column detector with the Helios 5CX illustrating excellent preservation of the neuropil. Select glutamate synapses labeled: axonal bouton (AB) directly apposed to a dendritic spine (S) containing an electron-dense PSD (asterisk). Additional neuropil components, such as astrocyte processes (As), myelinated axons (MA), and mitochondria (m) are also labeled. Scale bar is 10 μm in A and 3 μm in B.

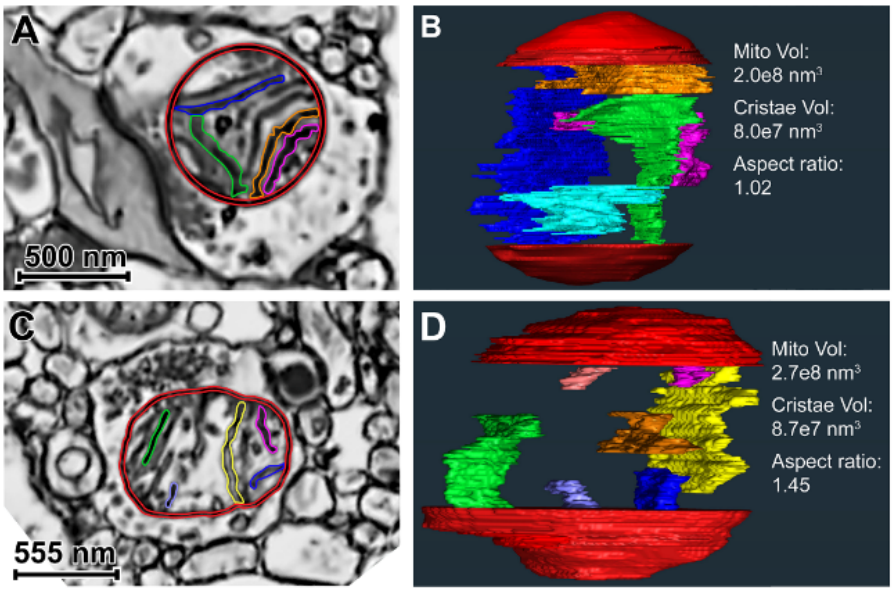

Figure 4. Single SEM images and 3D reconstructions illustrating globular and elongated presynaptic mitochondria in postmortem human DLPFC L3. A) Globular mitochondrion (red membrane; multiple-colored cristae). **B)** Internal view of the globular mitochondrion 3D reconstruction, including 5 cristae. Total mitochondrion and cristae volumes are provided. The aspect ratio is characteristic of globular morphology. **C)** Elongated mitochondrion (red membrane; multiple-colored cristae) present in a non-synaptic axon terminal. **D)** Internal view of the elongated mitochondrion 3D reconstruction, including 7 cristae. Quantitative values provided as described in B, and the aspect ratio is characteristic of elongated morphology. In B and D, only a subset of cristae volume reconstructions are shown in order to optimize visualization in a 2D image. In A and C, reconstructed cristae visible in the plane of view are colored.

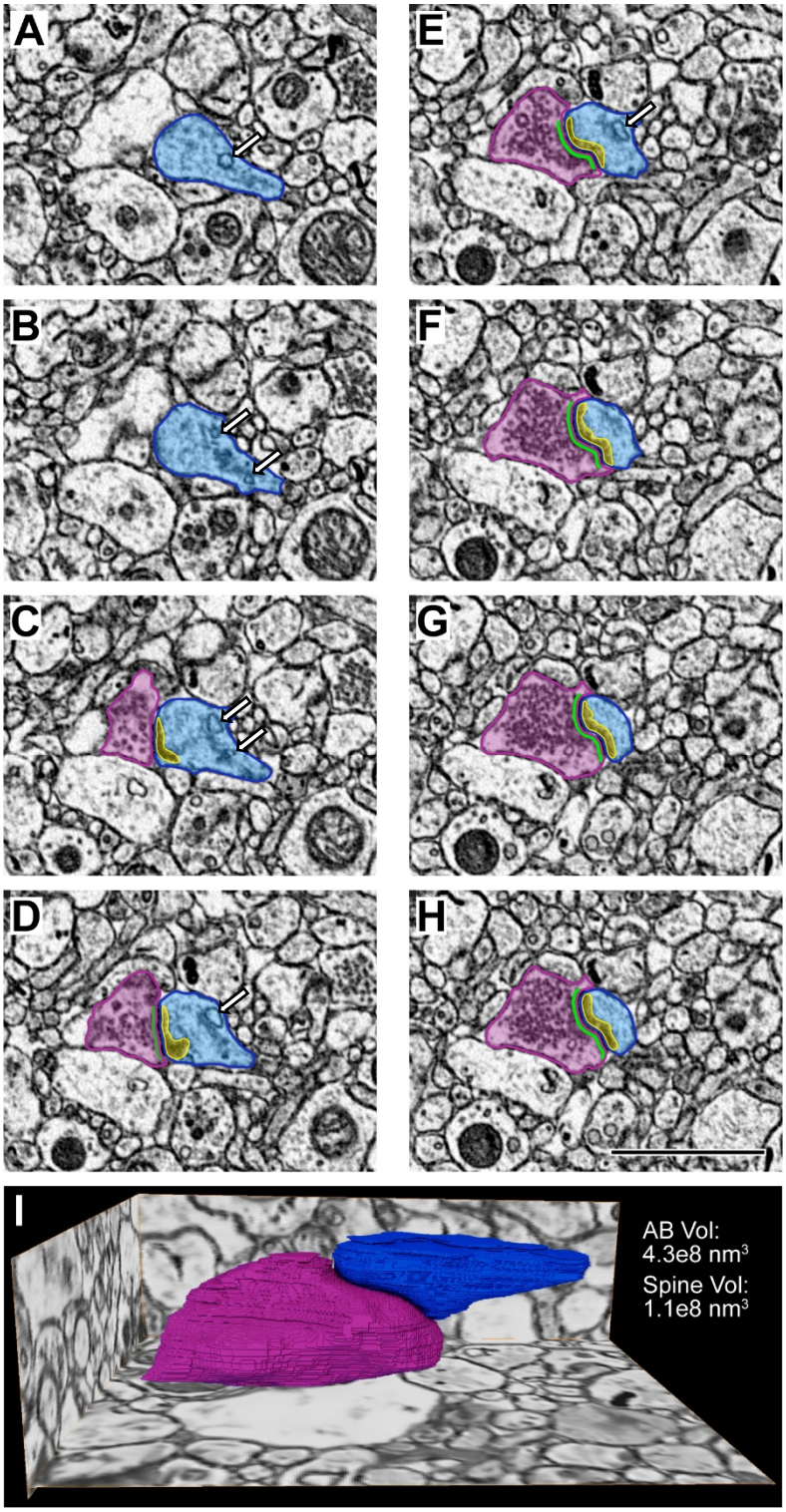

Figure 5. A series of electron micrographs viewed in the XY coordinate plane and the completed volume reconstructions of a Type 1 glutamatergic synapse in postmortem human DLPFC layer 3. A-H) Each panel represents 5 nm increments milled by the gallium FIB. In panels A-B, the dendritic spine (blue) is identified. Panel C is the initial visualization of the glutamatergic synaptic structure including a presynaptic axonal bouton (pink) with an active zone (green) and a postsynaptic spine (blue) containing a PSD (yellow). Note the presence of a spine apparatus (white arrow) in panels A-F. Scale bar is 2 mm. **I)** Glutamatergic synaptic structure reconstructed in 3D shown in the context of the surrounding tissue. Volume measurements for the axonal bouton (pink) and the spine (blue) are provided.

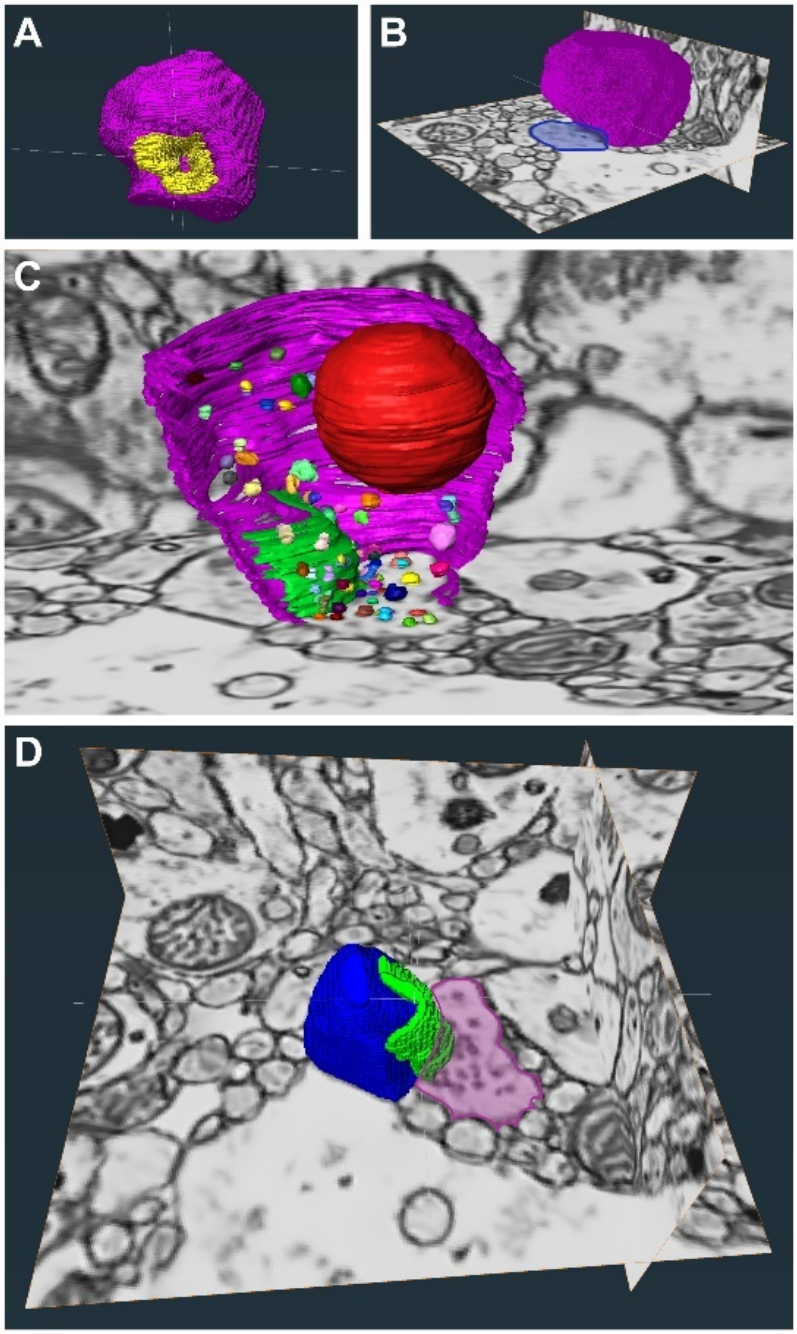

Figure 6. 3D reconstructions of synaptic and sub-synaptic structures in postmortem human DLPFC layer 3. A) Reconstructions illustrating relationships between the axonal bouton (pink) and PSD (yellow). The PSD morphology is perforated. **B)** Bouton reconstruction (pink) shown in the context of the surrounding tissue. The postsynaptic spine is labeled blue. **C)** Cross-sectional view of the bouton (pink) illustrating volume reconstructions of synaptic vesicles (multiple colors), a mitochondrion (red) and the active zone (green). **D)** Reconstructions illustrating the relationship between the spine (blue) and the active zone (green) located within the axonal bouton (pink).

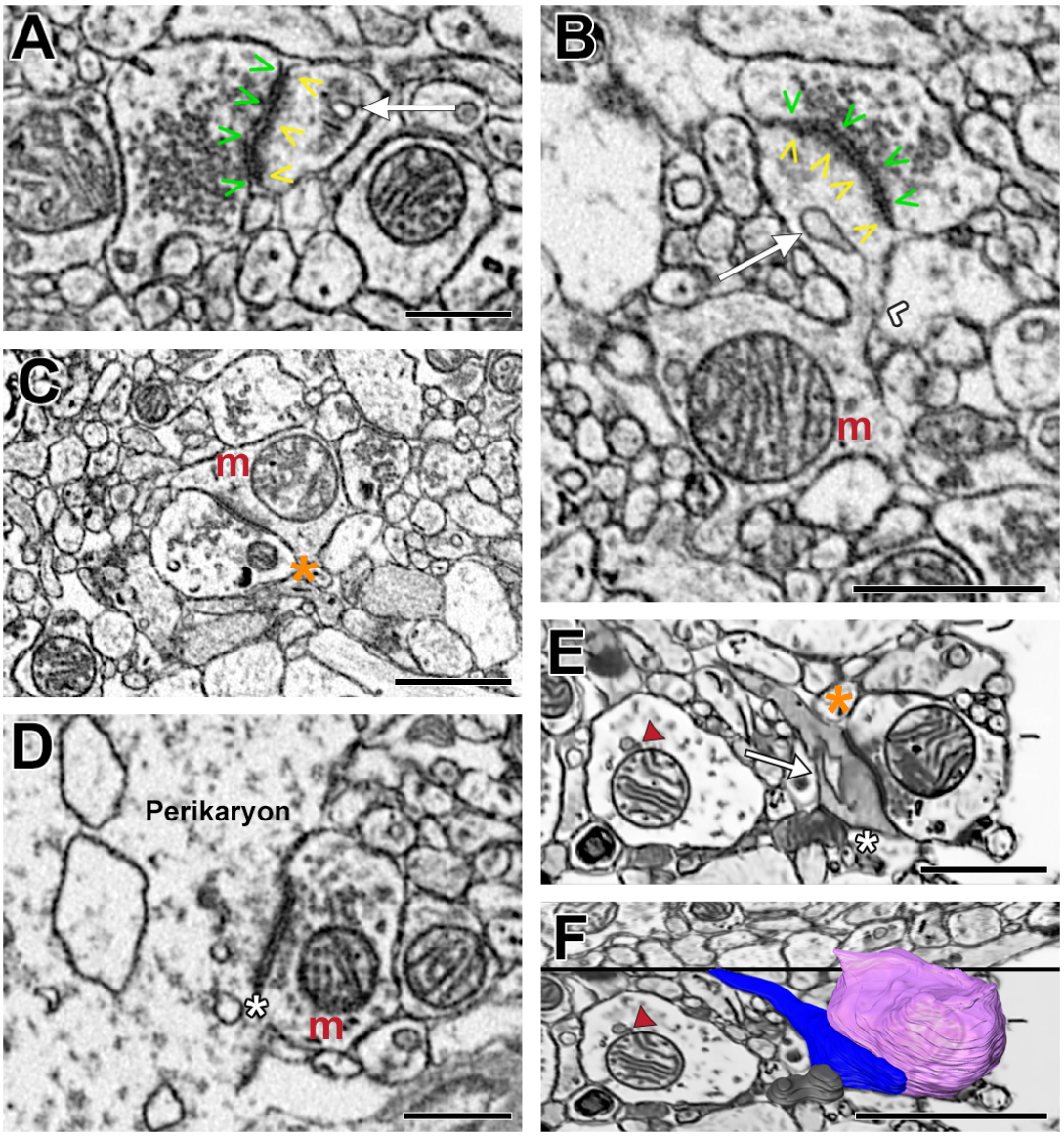

Figure 7. Representative images illustrating Type 1 and Type 2 synapses identified in in postmortem human DLPFC layer 3. A) Axonal bouton filled with synaptic vesicles and forming a Type 1 synapse onto a dendritic spine containing a spine apparatus. **B)** A parent dendritic shaft containing a mitochondrion positioned at the base of the spine neck. The spine head contains a spine apparatus and is receiving a Type 1 synapse. **C)** A bouton forming a Type 1 synapse onto a dendritic shaft containing a mitochondrion. **D)** Neuronal cell body receiving a Type 2, presumably GABAergic, synapse. **E)** A dendritic spine with a spine apparatus and electron-dense cytoplasm receiving a Type 1 and a Type 2 synapse. In the adjacent dendritic shaft, the mitochondrion is tethered to an electron dense vesicle. **F)** 3D reconstruction of the Type 1 bouton (pink), dendritic spine (blue) and the Type 2 bouton (grey) shown in E within the context of the 2D surrounding neuropil. **Symbol legend:** green arrowheads indicate the active zone; yellow arrowheads indicate the PSD; white arrow indicates the spine apparatus; white chevron indicates the spine neck; orange asterisk indicates a Type 1 synapse; white asterisk indicates a Type 2 synapse; red arrowhead indicates the mitochondrial-tethered vesicle. Scale bar is 1.5mm in A, B, D and F; and is 1mm in E.

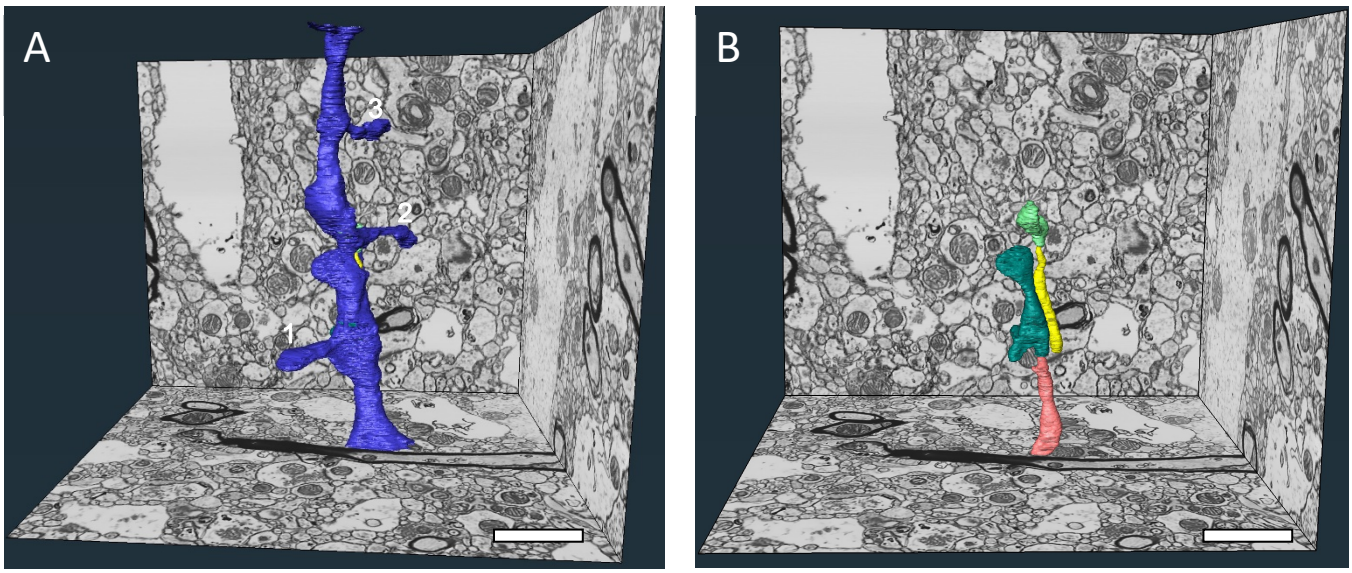

Figure 8. 3D reconstructions of a complex dendritic shaft with filopodia-like structures coursing through the dendritic cytoplasm. A) A perspective overview of a volume of DLPFC layer 3 with a dendritic shaft completely reconstructed. Multiple spines (numbered 1-3) protrude from the parent shaft, and the neck of a fourth spine is visible at the top of the volume. The mean shaft distance between spines is 2.0 ± 0.3 μm for a spine frequency of 0.5/mm of dendritic length. **B)** Similar perspective overview illustrating the four structures (salmon, teal, yellow and lime green) completely enveloped within the cytoplasm of the dendritic shaft. The yellow, teal and lime green axons are fully contained within the volume and are not connected to any surrounding structure. The entirety of the salmon axon is not included in the total volume. Scale bars are 2 μm.

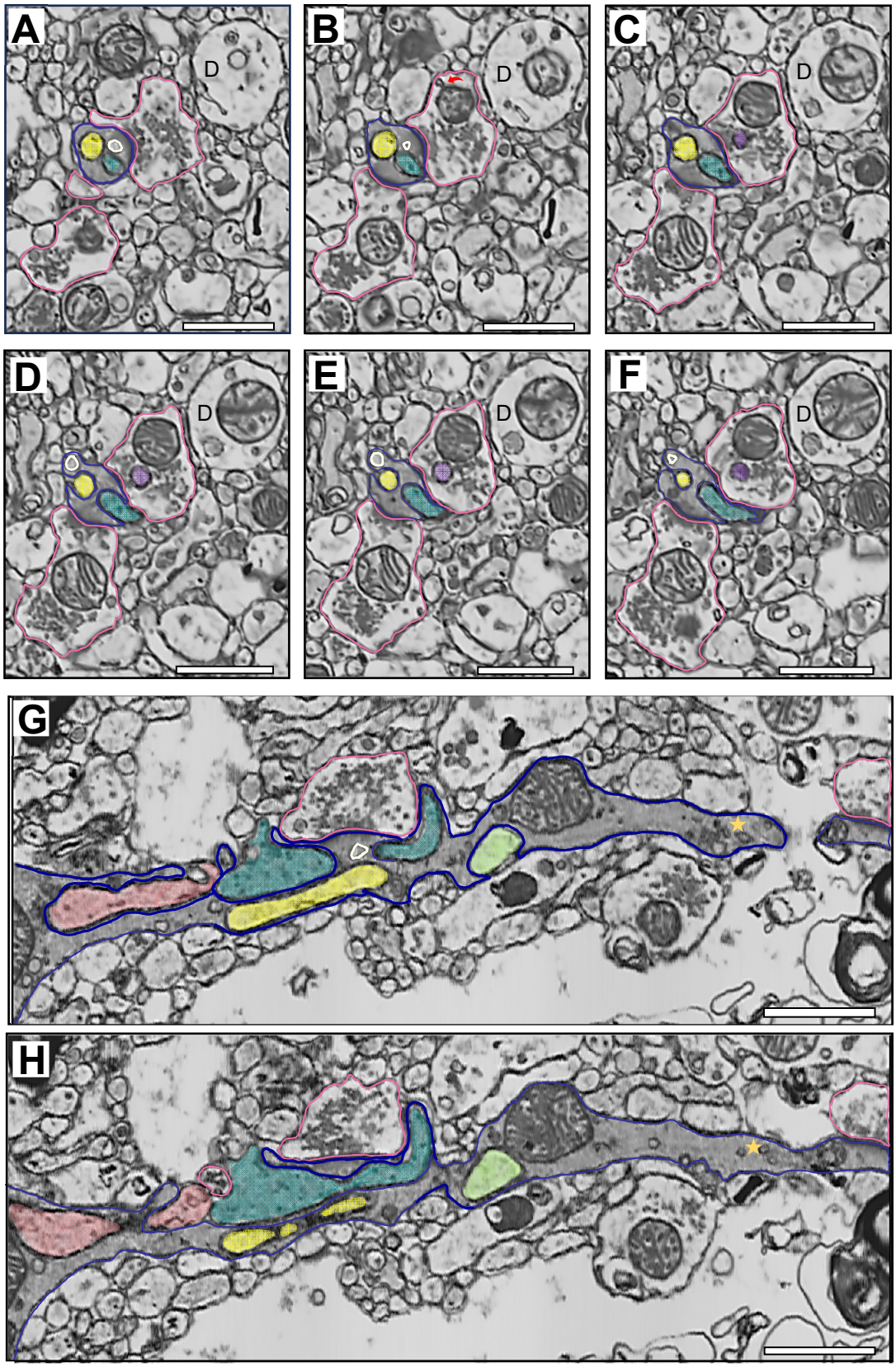
A
D
B
D
C
D
D
D
E
D
F
D
G
H

Figure 9. A series of electron micrographs viewed in different coordinate planes illustrating the unique ultrastructural features of the complex dendritic shaft. A-F) Electron micrographs spanning 315 nm in the XY coordinate plane illustrating two filopodia-like, invaginated structures (yellow and teal filled) completely enveloped within the dendritic shaft (dark blue outline) cytoplasm. The plasma membrane of the invaginated structures and the plasma membrane enclosing the dendritic cytoplasm are clearly distinct, and also show discrete, electron-dense regions which appear to be non-synaptic contacts. Unlike other dendritic profiles (D) in close proximity, the complex dendritic shaft exhibits an electron dense cytoplasm, indicative of an abundance of molecules involved in cellular, organelle and synaptic function. In Panel A, a single Type 1 synapse from an axonal bouton (pink outlined) is visible. Presumptive endosome large vesicle (ivory outlined) is positioned between the PSD and the two invaginated structures. In Panel B, an additional Type 1 synapse is present on the dendritic shaft. In the top bouton, a mitochondrial-derived vesicle (red curved arrow) is visible. Panels C-F illustrate the teal invaginated structure exiting the dendritic shaft, and the yellow structure partially exposed to the neuropil. Panels D-E also show an invaginated structure (purple filled) piercing the cytoplasm of the top synaptic axonal bouton. **G-H)** Electron micrographs separated by 70 nm in the XZ coordinate plane illustrating the same dendritic shaft, the Type 1 synapse initially present in Panel A, and all four filopodia-like invaginated structures (salmon, teal, yellow, and lime green filled). The electron-dense cytoplasm is apparent, as is an abundance of putative endosomal and SER structures. A classic example of amorphous vesicular clumps (gold star) is present in the dendritic shaft. Amorphous vesicular clumps likely reflect a mix of SER and endosomal vesicles (Cooney et al 2002). The yellow and teal invaginated structures and the endosome large vesicle (ivory outlined) are visible in Panel G, positioned centrally to the PSD. D- dendrite. Scale bar is 1 μm.

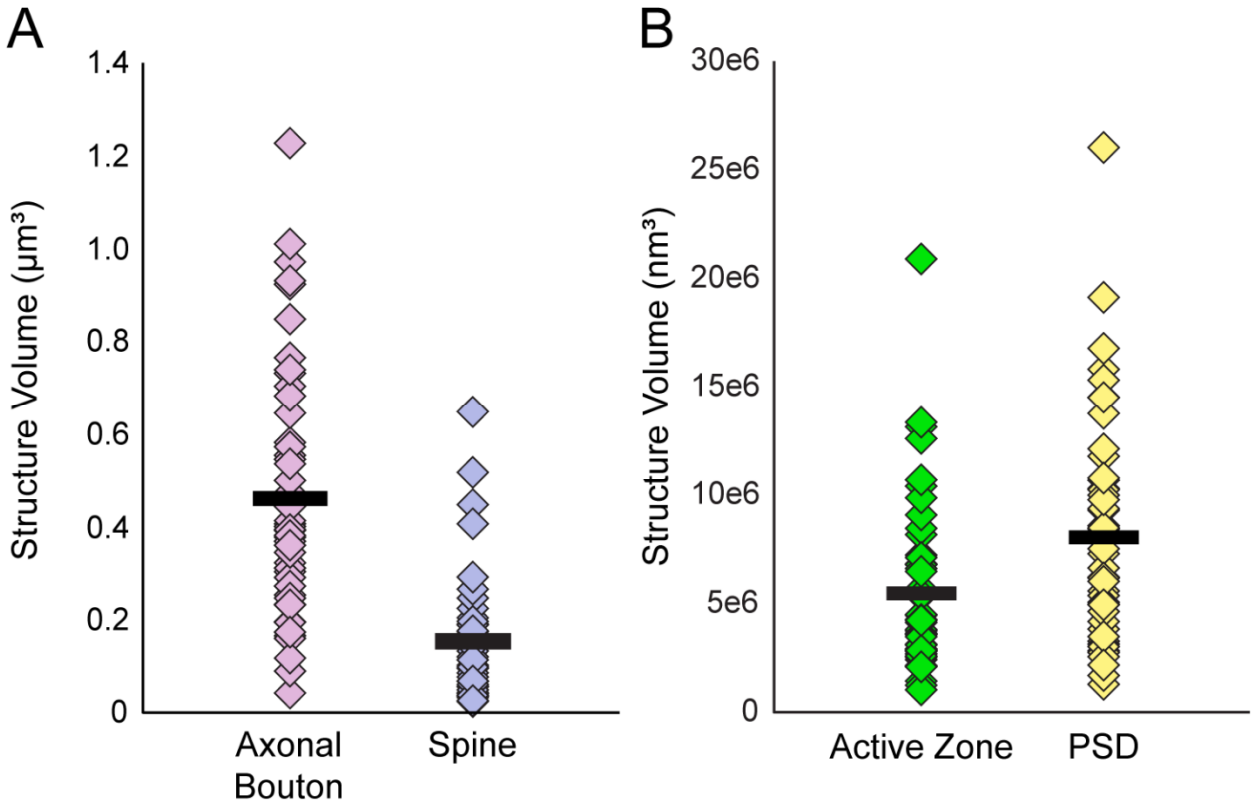

Figure 10. Scatter plots showing the volumes of each reconstructed synaptic and sub-synaptic structure in postmortem human DLPFC layer 3. A) Volumes of 50, Type 1 synaptic axonal boutons and the 50 postsynaptic spines. **B)** Volumes of the presynaptic active zones and PSDs. Markers represent an individual structure, and black bars represent the mean volume.

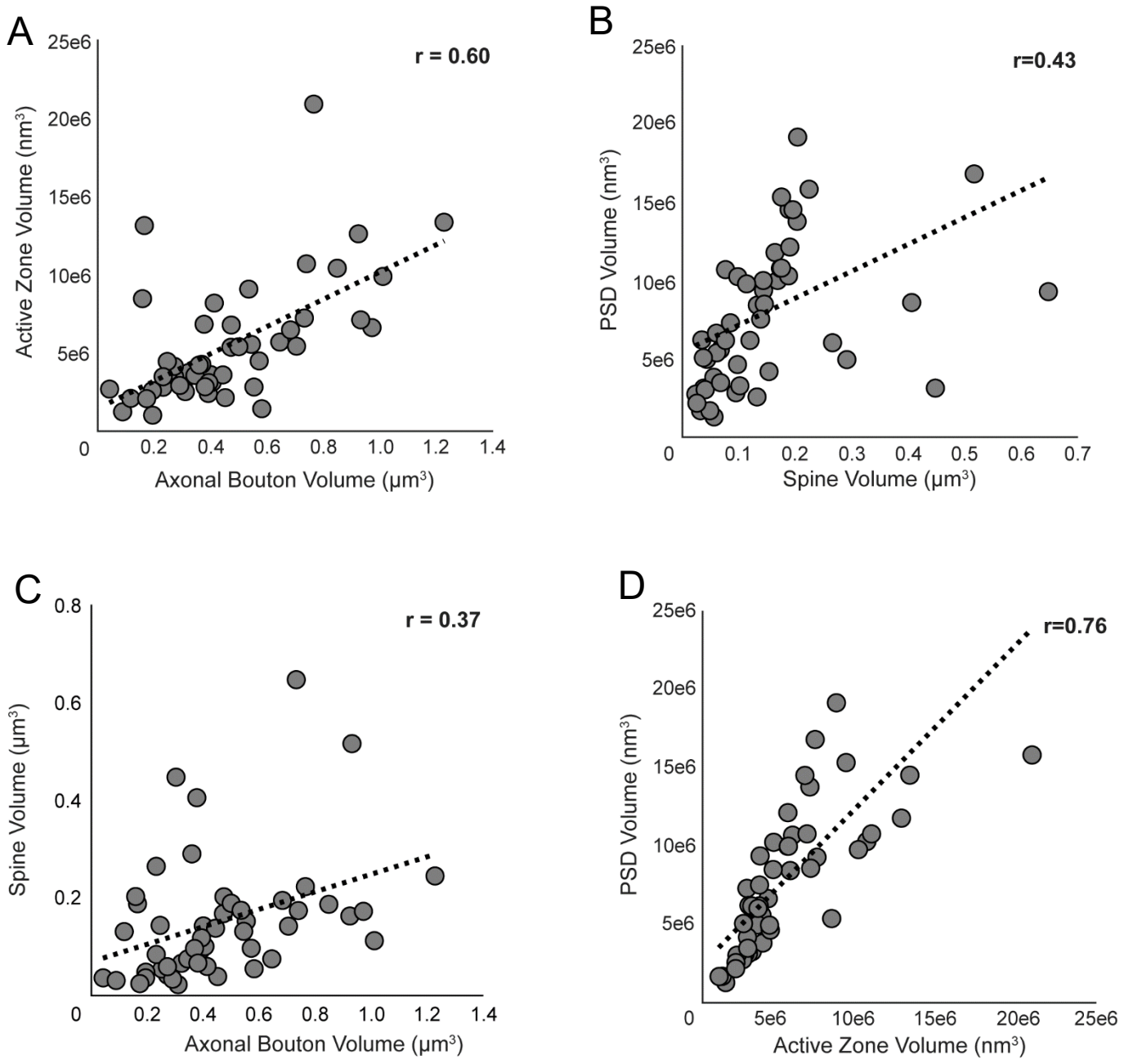

Figure 11. Correlation plots showing the relationships between Type 1 synaptic and sub-synaptic structures in postmortem human DLPFC layer 3. A-D) Markers represent the volumes of each structure within an individual synapse. Strong, positive correlations were identified between bouton and active zone volumes **(A)** and active zone and PSD volumes **(D)**. Moderate, positive correlations were identified between spine and PSD volumes **(B)** and bouton and spine volumes **(C)**.